Simultaneous observations of aerosol–cloud–albedo interactions with three stacked unmanned aerial vehicles

G. C. Roberts†, M. V. Ramana, C. Corrigan, D. Kim, and V. Ramanathan†

Center for Atmospheric Sciences, Scripps Institution of Oceanography, 9500 Gilman Drive, La Jolla, CA 92093

Contributed by V. Ramanathan, November 1, 2007 (sent for review August 14, 2007)

Aerosol impacts on climate change are still poorly understood, in part, because the few observations and methods for detecting their effects are not well established. For the first time, the enhancement in cloud albedo is directly measured on a cloud-by-cloud basis and linked to increasing aerosol concentrations by using multiple autonomous unmanned aerial vehicles to simultaneously observe the cloud microphysics, vertical aerosol distribution, and associated solar radiative fluxes. In the presence of long-range transport of dust and anthropogenic pollution, the trade cumuli have higher droplet concentrations and are on average brighter. Our observations suggest a higher sensitivity of radiative forcing by trade cumuli to increases in cloud droplet concentrations than previously reported owing to a constrained droplet radius such that increases in droplet concentrations also increase cloud liquid water content. This aerosol-cloud forcing efficiency is as much as −60 W m^{-2} per 100% percent cloud fraction for a doubling of droplet concentrations and associated increase of liquid water content. Finally, we develop a strategy for detecting aerosol–cloud interactions based on a nondimensional scaling analysis that relates the contribution of single clouds to albedo measurements and illustrates the significance of characterizing cloud morphology in resolving radiometric measurements. This study demonstrates that aerosol–cloud–albedo interactions can be directly observed by simultaneous observations below, in, and above the clouds.

autonomous unmanned aerial vehicle | cloud condensation nuclei | indirect effect | Maldives AUAV Campaign | long-range transport

Since the introduction of the Intergovernmental Panel on Climate Change (IPCC) nearly two decades ago, the uncertainty of the impact of anthropogenic aerosols has remained the least constrained radiative forcing component in understanding global climate change. Aerosols are generally considered to exert a cooling effect at the earth's surface by directly scattering incoming solar radiation back to space (1) or influencing cloud properties such as enhancing cloud albedo (2) and lifetime (3). For the first time, the IPCC 2007 assessment (4) provides a best estimate for the aerosol direct and indirect effects (-0.5 ± 0.4 and $-0.7^{+0.4}_{-1.1}$ W m^{-2} globally, respectively); however, the magnitude of the uncertainty is still more than a factor of 2 greater than those estimates and is still greater than the sum of uncertainties of all other components contributing to climate forcing (i.e., greenhouse gases, ozone, surface albedo, and solar irradiance).

The effect of aerosols on cloud microphysical and radiometric properties, known as the "indirect effect," consists of a two-part challenge—(*i*) response of cloud droplet number, n_D, and cloud liquid water path to a change in aerosols and (*ii*) response of cloud albedo, α_c, caused by changes in cloud microphysical properties. Aerosols are linked to cloud droplet formation by their physicochemical properties (5) and cloud dynamics such as updraft velocity (6), entrainment (7), and precipitation (3); whereas cloud radiative properties are determined by the number and size distribution of droplets and the cloud's geometric thickness (2). Numerous studies have demonstrated that an increase in aerosols increases n_D (8–12); however, fewer have actually measured the impact of aerosols on α_c (13, 14). Several studies have not detected the expected effect of aerosols on clouds, possibly because of variations in liquid water path (15–17), and employ aerosol and cloud properties in radiative transfer models to estimate radiative forcing.

The two analytical expressions given below illustrate the dependence of cloud optical depth, τ_c, and cloud albedo, α_c, on the cloud liquid water content, *lwc*; the effective radius, R_{eff}; the height of the cloud, h; the density of water, ρ_w; and an asymmetry parameter, g, for scattering of radiation by clouds.

$$\tau_c = \frac{3\, lwc\, h}{2R_{\text{eff}}\rho_w} \quad [1]$$

$$\alpha_c = \frac{(1-g)\tau_c}{2+(1-g)\tau_c}. \quad [2]$$

Eq. **2** is a highly simplified expression that is derived by employing the two-stream approximation (18) to the radiative transfer equation and by assuming that the drops do not absorb solar radiation. Neither of the two simplified expressions nor the assumptions used to derive them are used in sophisticated modeling studies, but are written here to convey the essential physics of the aerosol–cloud interactions.

To this end, the Maldives AUAV Campaign (MAC) demonstrates the ability to observe aerosol and cloud microphysical properties and solar radiation fluxes simultaneously by using emerging technology (i.e., autonomous unmanned aerial vehicles, AUAVs) as new tools in atmospheric sciences (19). The MAC results presented here demonstrate that it is possible to directly observe the aerosol–cloud–albedo interactions and establish the link between aerosols and clouds—and ultimately, between changes in aerosols and subsequent changes in cloud radiative properties. We also compare the relative contribution of the aerosol direct and indirect effects, deduced directly from aircraft measurements to demonstrate the capabilities of a new observing system for addressing long-standing problems in atmospheric sciences.

Results

Part I: Aerosol–Cloud Relationship. MAC is characterized by the arrival of a persistent, elevated aerosol layer to an already polluted boundary layer and is categorized into two periods based on vertical profiles of aerosols and key atmospheric state parameters (Fig. 1; Table 1). During period I of the experiment, aerosol transport is mostly confined to the boundary layer (<1,000 m above sea level,

Author contributions: G.C.R. and V.R. designed research; G.C.R., M.V.R., C.C., D.K., and V.R. performed research; G.C.R. and D.K. contributed new reagents/analytical tools; G.C.R., C.C., and M.V.R. analyzed data; and G.C.R. and V.R. wrote the paper.

The authors declare no conflict of interest.

†To whom correspondence may be addressed. E-mail: gcroberts@ucsd.edu or vramanathan@ucsd.edu.

This article contains supporting information online at www.pnas.org/cgi/content/full/0710308105/DCSupplemental.

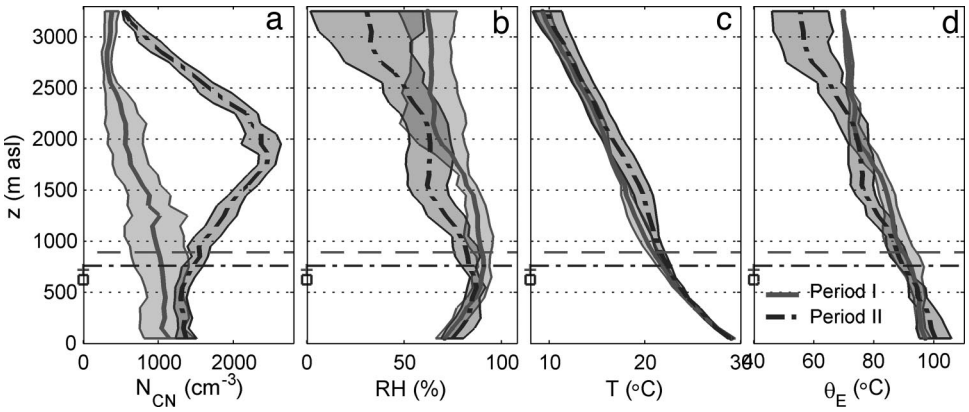

Fig. 1. Vertical profiles of total aerosol concentration (*a*), relative humidity (*b*), temperature (*c*), and equivalent potential temperature (*d*) are shown for each period. Thick lines show average profiles and shading designates 1-σ variability. Horizontal dashed lines show average sampling altitudes of the in-cloud AUAV. Lifting condensation levels (LCLs) are shown by plus (period I) and square (period II) markers on left axes.

masl), whereas period II is characterized by an aerosol layer that peaks at 2,000 masl (≈2,500 cm^{-3}). Aerosol concentrations, N_{CN}, at the surface are relatively high in both periods (1,000–1,250 cm^{-3}) compared with clean marine conditions of a few hundred cm^{-3} (20). Wind fields above the boundary layer (850 mbar) change from an easterly flow south of the Maldives associated with the Intertropical Convergence Zone (ITCZ) to a northwesterly flow that carries long-range transport of pollution to the Maldives from the Arabian Peninsula and South Asia. Although N_{CN} in the boundary layer does not significantly change on the arrival of the elevated layer, the new aerosol (presumably aged anthropogenic emissions and dust) causes a shift in the size distribution at the surface and aloft (21), and doubles the accumulation mode diameter (Fig. 2*a*). Such a shift in aerosol size distributions affects the subset of aerosols that serve as seeds for cloud formation, i.e., cloud condensation nuclei (CCN). Indeed, the CCN spectra change, especially at low S_c, as concentrations at 0.1% S_c, $N_{CCN\_0.1}$, and increase by 60% in period II (Fig. 2*b*; Table 1). Activation indices, the ratio of the observed critical diameter to that of a soluble salt (22), were close to unity at 0.1% S_c in both periods, indicating that activated particles contain a large soluble fraction. The CCN spectra approach the soluble limit at lower supersaturations (Fig. 2*b*) implying that chemical composition changes as a function of size probably because of cloud processing or contributions from sea salt.

Although the indirect effect relates change in cloud albedo to the input of aerosol, the first challenge is to establish the connection between cloud microphysical properties and aerosol number concentrations, in particular, CCN. Vertical profiles of aerosols and comparisons with ground observations at MCOH (Fig. 1) indicate a well mixed boundary layer, which allows a reasonable comparison between ground-based CCN measurements and cloud observations (23, 24). The MAC observations show a ≈40% increase in n_D during period II, which is inextricably linked to the change in aerosol properties (25) (i.e., shift in size distribution) and enhancement in $N_{CCN\_0.1}$ (Fig. 3). $N_{CCN\_0.1}$ correlate to maximum cloud droplet concentrations, $n_{D,max}$ ($r^2 = 0.62$; Fig. 3); however, the correlation is stronger during period I ($r^2 = 0.89$) when a $N_{CCN\_0.1}$:$n_{D,max}$ ratio of 0.86 ± 0.09 indicates peak in-cloud S_c close to 0.1%. Changes in aerosol properties increase n_D in period II, and the $N_{CCN\_0.1}$:$n_{D,max}$ ratio decreases (0.63 ± 0.09), which is indicative of lower in-cloud S_c. The marked difference in the $N_{CCN\_0.1}$:$n_{D,max}$ relationship between the periods suggests more competition for water vapor during period II either from enhancement of CCN that activate at lower S_c, changes in vertical velocity, or entrainment of drier air from the aerosol layer above the clouds.

Part II: Cloud–Albedo Relationship. The results in part I establish the link between aerosols (particularly CCN) and n_D; yet, the second and more difficult part in assessing aerosol–cloud interactions is relating changes in microphysical properties to changes in cloud albedo, α_c—a central requirement for understanding the aerosol indirect effect. Through coordinated, stacked flights

Table 1. Average aerosol and cloud properties for each sample period.

Period	I	II
Dates	March 6–19	March 20–28
Back trajectory (3,000 masl)	Marine recirculation	Arabian Peninsula and India
Flight	1, 4, 5, 7	9, 10, 11, 12, 13, 14
Distance, km	1,125	1,690
Cloud fraction, %	6.7 ± 2.3	5.0 ± 2.0
n_D, cm^{-3}	205 ± 124 [186 ± 117]	284 ± 150 [359 ± 189]
$n_{D,max}$, cm^{-3}	411 ± 265 [361 ± 249]	551 ± 251 [665 ± 356]
R_{eff}, μm	6.74 ± 0.62 [7.0 ± 0.48]	6.45 ± 0.46 [6.56 ± 0.45]
Cloud events	144 [23]	96 [34]
Cloud width, m	423 ± 333 [295 ± 199]	401 ± 277 [299 ± 143]
lwc, g·m^{-3}	0.26 ± 0.19 [0.25 ± 0.18]	0.31 ± 0.20 [0.41 ± 0.25]
N_{CN}, cm^{-3}	1269 ± 622	1255 ± 258
$N_{CCN\_0.1}$, cm^{-3}	502 ± 113	812 ± 54
α (clear-sky; 3,000 masl)	0.067 ± 0.003	0.079 ± 0.006

Variations reported as 1-σ. In-cloud transit distance determines cloud width. Brackets denote stacked flight averages used in analysis of Fig. 5.

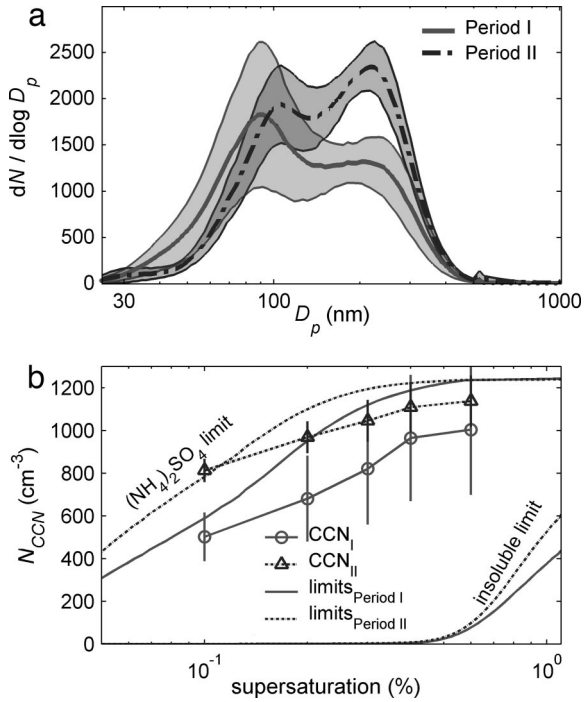

Fig. 2. Aerosol size distributions (*a*) and CCN spectra (*b*) at MCOH during periods I and II. Calculated CCN spectra for soluble [i.e., $(NH_4)_2SO_4$] and insoluble limits based on aerosol size distributions in *a* are also shown in *b*. D_p is the dry diameter.

using three AUAVs—one sampling at cloud level and the other two above the clouds—radiometric and microphysical properties of individual clouds were simultaneously observed. We use a detailed analysis of a single cloud [Fig. 4 and supporting information (SI) Fig. S1] to illustrate the simultaneous α_c response at different altitudes. In addressing the effects of aerosols on cloud optical properties, this analysis introduces a scaling function (see *SI Text*, Eq. **S7**, Fig. S2), which demonstrates the importance of cloud morphology in interpreting albedo measurements.

In the case study (Fig. 4), the in-cloud AUAV (at 796 masl) flew through a cloud and measured an average n_D and effective radius, R_{eff}, of 372 ± 236 cm^{-3} and 6.8 ± 0.6 μm, respectively. The average *lwc* is calculated to be 0.49 ± 0.34 $g{\cdot}m^{-3}$. At the same time, both AUAVs above the cloud (at 1,625 and 3,250 masl) captured the radiometric response of the same cloud element. The up-welling

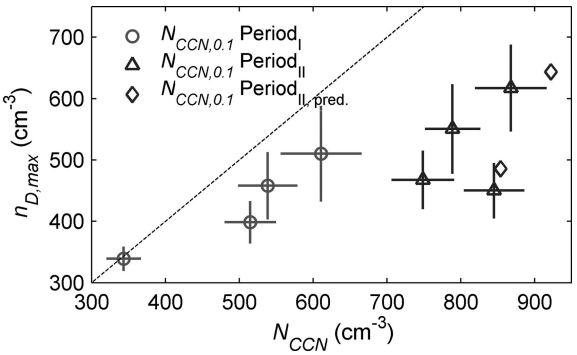

Fig. 3. Relationship between flight rms-averaged CCN concentrations (at 0.1% S_c; $N_{CCN,0.1}$) and maximum in-cloud droplet concentrations ($n_{D,max}$) for all cloud flights. Diamonds indicate simulated $N_{CCN,0.1}$ in period II based on aerosol size distributions and assumed chemistry. The dashed line represents the 1:1 correlation.

broadband pyranometers on the middle and upper AUAVs measured a net increase of 183 ± 3 W m^{-2} and 16 ± 1 W m^{-2}, respectively, which translates to an maximum increase in measured albedo, α_m, of 0.168 ± 0.002 and 0.010 ± 0.003 compared with the cloud-free background. Most of the increase in α_m is because of the cloud directly below the AUAVs; however, the ocean, islands, and other clouds in the region also contribute. A camera, mounted on the in-cloud AUAV illustrates the complicated 3D structure (Fig. S1) and shows several smaller clouds in the immediate vicinity of the main cloud. By using the onboard image, we estimate the cloud top and width to be ≈1,250 masl and 500 m and use this spatial information to simulate the expected albedo response of both above-cloud AUAVs based on the scaling relationship (see *Discussion*). The cloud optical depth (τ_c = 70 ± 49) is estimated from Eq. **1** (h = 650 ± 50 m assuming vertically homogeneous *lwc*), which yields α_c = 0.826 ± 0.10 (Eq. **2**) by using an asymmetry parameter (g = 0.865) from Indian Ocean Experiment (INDOEX) observations of trade cu (26). Although we cannot conduct an exact closure between cloud properties and radiometric response (precise measurements of the 3D structure are needed), a simple pixel plane-parallel radiation model shows relatively good agreement with the measured enhancement in albedo at both altitudes. The different simulations in Fig. 4 show the expected albedo response for best estimates of cloud height and width—1,200 masl cloud top and 600 m cloud width correlates well with both AUAV observations—and compare changes in spatial relationships (i.e., cloud morphology) to changes in cloud optical properties (i.e., an enhancement in α_c by 0.2). The main discrepancy between measured and simulated values of the radiometric response is caused by the uncertainty in the cloud morphology. These results emphasize the complexity in detecting the indirect effect and show that aerosol–cloud effects can easily be masked by uncharacterized differences in cloud morphology.

By using the measurements for all stacked flights, data from 41 individual trade cu were analyzed to determine the effect of n_D (and *lwc*) on α_c at 1,600 masl (Fig. 5). The analysis only includes cases when the down-welling flux was constant (i.e., no clouds overhead), clouds were separated by at least 60 s (to avoid influence from neighboring clouds), and solar zenith angles <30° (to minimize uncertainties in zenith angle corrections). Despite variability in cloud geometric thickness, we observe an enhancement in the maximum observed albedo above a cloud, $\alpha_{m,pk}$, with increasing n_D and *lwc* ($r^2 > 0.468$; Fig. 5). Observations of these 41 samples show nearly a twofold increase in average n_D and *lwc* (Table 1; values in brackets) and resulting $\Delta\alpha_{m,pk}$ = 0.01 (0.0199 ± 0.003 to 0.0303 ± 0.006 rms in periods I and II). There is little correlation between $\alpha_{m,pk}$ and cloud width (r^2 = 0.093; derived from in-cloud transit distance) and the influence of neighboring clouds is negligible because of the low cloud fraction.

Based on differences of n_D and *lwc* for these 41 samples (Table 1; values in brackets), the expected change in cloud albedo or albedo susceptibility, $\Delta\alpha_c$,

$$\Delta\alpha_c = \frac{\alpha_c\,(1-\alpha_c)}{3}\left[\frac{\Delta n_D}{n_D} + 2\,\frac{\Delta lwc}{lwc} + 3\,\frac{\Delta h}{h}\right] \qquad [3]$$

is ≈0.16 ± 0.03 ($h \approx 600$ m and $\Delta h\, h^{-1} = 0$; see *SI Text*, Eq. **S13** for derivation).

Because the MAC observations were made several hundred meters above the cloud tops, relating the observed $\Delta\alpha_{m,pk}$ = 0.01 (Fig. 5) to $\Delta\alpha_c$ requires information about the size of the cloud (including 3D information) and its distance to the above-cloud AUAV. The nondimensional change in albedo (Eq. **5**) for these 41 samples, $\alpha_* = \Delta\alpha_{m,pk}\,\Delta\alpha_c^{-1}$ = 0.01/0.16 = 0.063 ± 0.044, corresponds to measurements 600 m above cloud top (between 400 and 1,000 m when accounting for the uncertainty), which is in general agreement with experimental conditions (Fig. 1).

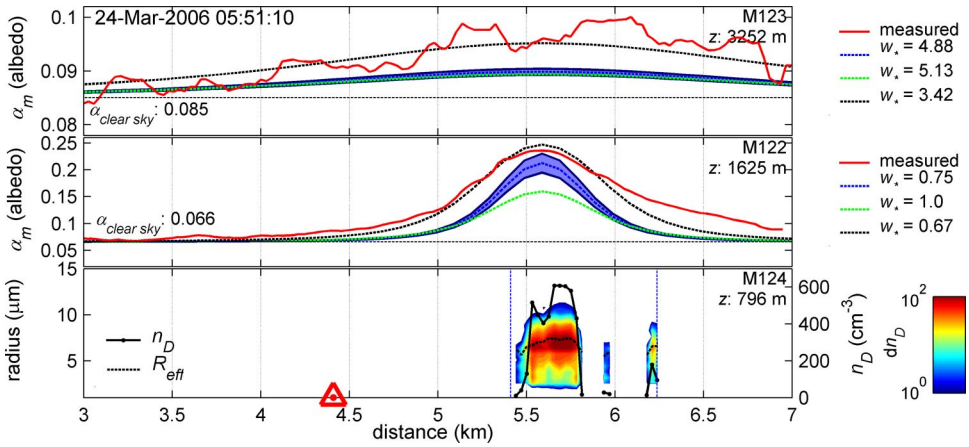

Fig. 4. Distance along flight track showing the simultaneous measurements of cloud microphysical and radiometric properties from three AUAVs at different altitudes. The in-cloud measurements (n_D, R_{eff}, and droplet distribution) are shown in *Bottom*. The observed broadband albedo (0.3–2.8 μm) is shown by the red line in *Top* and *Middle*. Model response in *Top* are calculated based on characteristic length, w_*, and cloud albedo, $\alpha_c = 0.826$—black and green dashed lines from 1,200 masl cloud top and 600 and 400 m cloud width, respectively; blue dashed line from 1,300 masl cloud top and 400 m cloud width. The shaded blue region illustrates $\Delta\alpha_c \pm 0.1$. Thin horizontal dashed lines show the minimum albedo during the leg. Altitudes for the AUAVs are shown in each profile. The red marker in *Bottom* shows the location of the AUAV for the image in Fig. S1.

Studies of shiptracks (27) have shown satisfactory agreement with $\Delta\alpha_c$ and report a weak correlation between *lwc* and n_D which removes the $2\Delta lwc/lwc^{-1}$ and $3\Delta h/h$ term in Eq. **3**. Nonetheless, Platnick and Twomey (28) point out an enhanced susceptibility when an increase in n_D is also accompanied by an increase in *lwc*. Our results suggest trade cu α_c is about a factor of 3 more susceptible to changes in n_D than previous estimates because of the strong correlation between n_D and *lwc*. In addition, simulations have suggested that h may increase or decrease with n_D (29, 30). However, the $\Delta\alpha_c$ effect of a 15% change in h (29) is still seven times less than the doubling of n_D for MAC conditions.

Cloud Properties. Trade cu sampled during MAC are similar to nonprecipitating clouds observed during INDOEX (31) categorized as "transitional" and "polluted" with $R_{eff} < 10$ μm and cloud widths of several hundred meters (20). However, an interesting distinction of trade cu observed during MAC is the strong correlation between n_D and *lwc* ($r^2 = 0.85$; Fig. 6); which constrains the variability in R_{eff}. R_{eff} is independent of n_D ($r^2 = 0.09$) and cloud width ($r^2 = 0.01$). Similar results (32, 33) point to inhomogeneous mixing where evaporation timescales are much shorter than those of turbulent mixing allowing some of the droplets to be completely evaporated (34, 35). Vertical profiles of trade cu show subadiabatic *lwc* (Fig. 7), where a slight increase in R_{eff} is negated by a decrease in n_D. The linear trend between n_D and *lwc* is consistent throughout MAC, supporting conclusions that changes in aerosols dominate the variability in τ_c for a similar thermodynamic environment.

In period II, there is more water vapor available for condensation and a slightly less stable boundary layer, which is consistent with Table 1 and the lower lifting condensation level (LCL) in Fig. 1. Nonetheless, MAC observations show a 15% lower *lwc* for the same n_D in period II because of a slight decrease in R_{eff}. Vertical profiles of relative humidity (Fig. 1*b*) show drier air above the clouds in

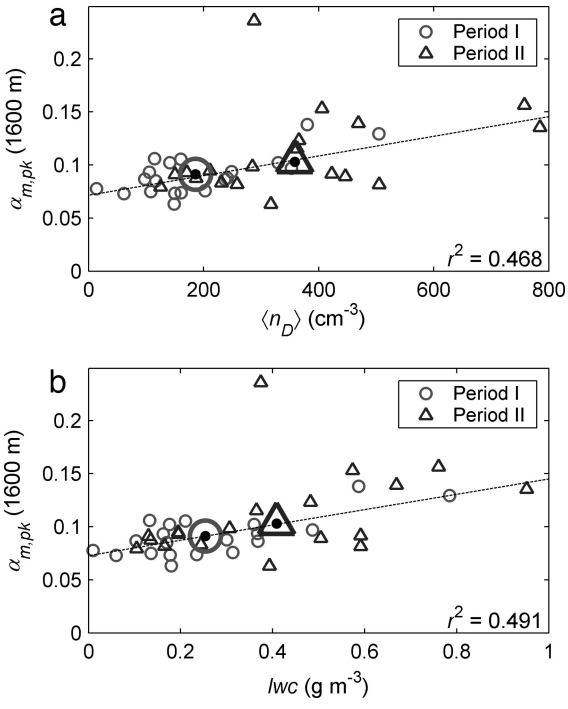

Fig. 5. Relationship between maximum measured albedo, $\alpha_{m,pk}$, at 1,600 masl for 41 clouds and simultaneous observations of average n_D and *lwc*. The large markers with a center black dot denote the period averages in brackets in Table 1. The single anomalous point in period II ($\alpha_{m,pk} \approx 0.23$) is not included in the average.

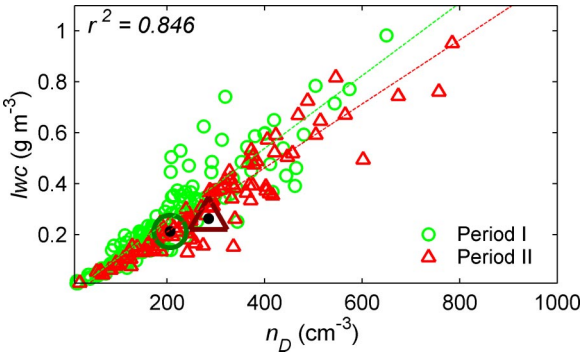

Fig. 6. Relationships between n_D and *lwc* for all clouds sampled during MAC. Dashed lines represent robust fits for each period. Green and red markers represent periods I and II, respectivley. The large markers with a center black dot illustrate the period averages.

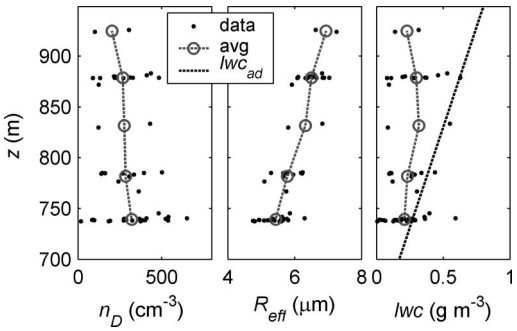

Fig. 7. Vertical profiles of n_D (*Left*), R_{eff} (*Center*), and *lwc* (*Right*) of trade cu during flight 18. The thin dashed line illustrates the expected *lwc* profile for an adiabatic cloud, lwc_{ad}.

period II, consistent with simulations of trade cu that entrainment of dry air above the clouds exerts a strong influence on *lwc* (36).

Discussion

Scaling Analysis. Discerning subtle changes in α_c from surface heterogeneities and surrounding clouds requires an understanding of the spatial scales of the earth's surface and clouds relative to the height of the measurement. Sensors with a cosine response (i.e., pyranometers) receive a greater contribution of their signal from objects that are closer and normal to the sensor as demonstrated by the two AUAVs flying above the cloud at different altitudes in Fig. 4. The observed response, α_m, is related to a single cloud of width, W, albedo, α_c, and its distance below the AUAV, z. The nondimensional response in albedo, α_*,

$$\alpha_* = \frac{\alpha_m}{\alpha_c} = h \int_0^{w/2} \frac{r}{(r^2 + z^2)^{3/2}}\, dr \qquad [4]$$

is calculated for a cloud projection that is plane-parallel and directly below the sensor. By integrating and substituting a nondimensional length, $w_* = z\ W^{-1}$, the scaling relationship becomes

$$\alpha_* = \frac{\alpha_m}{\alpha_c} = \frac{2w_*}{\sqrt{1 + 4w_*^2}} \qquad [5]$$

and provides the sampling constraints to detect relatively small changes related to aerosol indirect effects (Fig. S3). For example, the AUAVs in the above study (Fig. 4) sampled at characteristics lengths, $w_* \approx 0.75$ (1,625 masl) and 4.9 (3,250 masl), which translate to instrument responses of 17% and 0.5%, respectively (Eq. **5**) of the total change in α_c of the cloud below. Although the albedo measurements for both AUAVs show variations in the baseline up to ≈0.005 peak-to-peak, the maximum difference in α_m induced by $\Delta\alpha_c = 0.2$ is 0.03 and 0.001 (i.e., $0.2 \times 17\%$ and $0.2 \times 0.5\%$) for the middle and top AUAVs, respectively. The blue-shaded region in Fig. 4 denotes the expected changes in α_m related to aerosol–cloud interactions. $\Delta\alpha_c = 0.2$ corresponds to a factor of 2 increase in n_D and *lwc* (Table 1; Eq. **3**) between periods I and II. This case study shows that albedo measurements are sensitive to cloud morphology, particularly when the cloud element occupies a small fraction of the pyranometer's field of view. In addition, the variability in cloud properties (even those not along the flight track) needs to be fully characterized to quantify the contribution of each cloud element to α_m.

As cloud fraction increases, cloud–cloud radiative effects (37) may enhance the net reflected flux at intermediate cloud fractions. Contribution from neighboring clouds certainly influences the measured pyranometer signals as shown in the elevated signal after the main cloud in Fig. 4. Therefore, extrapolating the MAC results of trade cu to cloud systems with larger spatial scales is not so straightforward. Formation flights with manned aircraft over stratocumuli, SCu, in the Pacific Ocean have been conducted (38) with unexplained discrepancies between simulated and measured cloud albedos. In that experiment, a second aircraft flew 1 km above clouds. At this height above the clouds, 50% of the signal comes from a 3,000-m diameter region making it difficult to relate changes in α_m to variations in the cloud field. Simulations of unbroken marine SCu have shown that horizontal variability of α_c can vary by more than a factor of two because of changes in τ_c (39, 40). Because the horizontal variability scales to roughly twice the thickness of the cloud deck, nonlinear variability in α_c of surrounding cloud cells may mask the aerosol–cloud–albedo interactions on the larger scale of the cloud system.

Aerosol-Cloud Effect. The magnitude of the aerosol effect on cloud albedo, $\Delta F_{\text{aerosol-cloud}}$, from period I to II is estimated by

$$\Delta F_{\text{aerosol-cloud}} - F_0\ T_a^2\ f_c\ \Delta\alpha_c \qquad [6]$$

where F_o is the incident downward flux (incoming TOA diurnal average: ≈425 W m^{-2}), T_a is the transmittance through the atmosphere at 1,600 masl ($T_a = 0.925$), f_c is the cloud fraction during period II ($f_c = 0.05$), and $\Delta\alpha_c = 0.05$–0.16 (Table 1, values outside and in brackets). The observations measure an aerosol-cloud effect of -1 to -2.9 ± 0.7 W m^{-2}. The slight decrease in cloud fraction (from 6.7% to 5%) changes the forcing by ≈1 W m^{-2}; however, this decrease cannot be attributed to an aerosol effect and has been excluded to isolate the aerosol effect on cloud optical properties. By normalizing with respect to cloud fraction, the diurnal average top-of-atmosphere aerosol-cloud forcing efficiency is as much as -60 W m^{-2} per 100% cloud fraction for a doubling in n_D and associated increase in *lwc*. In comparison, clear-sky albedos increased from period I to period II because of the elevated pollution layer (Table 1)—the direct top-of-atmosphere effect of this elevated aerosol layer is -4.3 ± 2.5 W m^{-2}. These findings provide direct observations of the aerosol direct and indirect effects and a basis for reducing the uncertainty of anthropogenic aerosols as the least constrained radiative forcing component in understanding global climate change.

Materials and Methods. The MAC experiment was conducted from March 6 to 31, 2006, to observe long-range transport of dust and anthropogenic pollution from the Arabian Peninsula and South Asia (19). The observing system consists of three AUAVs in a synchronous vertical formation with miniaturized instruments for measuring aerosols, clouds, and radiometric fluxes (19). The stacked flights are programmed to autonomously sample the same vertical column below, in, and above the clouds to study how the boundary layer aerosols feeding the trade wind cumuli modify cloud microphysical and radiative properties. Vertical stacking was performed autonomously between 500 and 3,000 m and generally maintained <300 m horizontal separation, which translates to <10-s latency between the aircraft. See Movie S1 for a demonstration of the coordinated flight. The Maldives Climate Observatory on Hanimaadhoo Island (MCOH; 6.77°N; 73.18°E), a long-term monitoring station for the Atmospheric Brown Cloud (ABC) project (41, 42), serves to complement and validate the airborne measurements. In addition, a streamwise thermal-gradient CCN instrument (43) measured CCN spectra between 0.1% and 0.6% supersaturation, S_c, at MCOH.

Aerosol, cloud, radiometric instruments, and an integrated data acquisition system were deployed with a total payload weight and power <5 kg and 30 W, respectively. The AUAV payload is mission-specific and outfitted to perform a particular set of atmo-

spheric measurements. Much of the instrument suite includes commercially available instruments that have been repackaged or redesigned to minimize weight and volume. These measurements include aerosol number and size distribution, aerosol absorption, cloud drop size distribution, solar radiation fluxes (visible and broadband), temperature, pressure, and relative humidity. A shrouded aerosol inlet was designed to minimize aerosol sample biases. The data collected during MAC has been validated by using standard calibration routines in conjunction with comparisons to ground-based instruments in both laboratory and *in situ* settings.

The in-cloud platform measures cloud droplet number and size distributions of trade cu—and a real-time video camera assists in targeting the clouds. The aerosol-radiometric AUAVs (i.e., above and below cloud) measure aerosol concentrations, size distributions, and visible and near-IR absorption coefficients as well as broadband (0.3–2.8 μm) and visible (0.4–0.7 μm) albedo. Occasionally, the "below-cloud" AUAV flew above the clouds such that two AUAVs measure cloud albedo at different altitudes simultaneously. Radiometric data are corrected for pitch and roll and cloud albedos are normalized based on a clear sky model to remove solar zenith angle dependence (44). Only cases when the solar zenith angle is $<30°$ are used for this study to minimize 3D effects of trade cu on albedo measurements. Clear sky albedos were measured at 3,000 masl by averaging multiple consecutive legs where no clouds were sampled and the observed albedo did not change. Cloud events are counted when droplet concentrations, n_D, exceed a threshold (7 cm^{-3}) for at least 3 s (i.e., cloud width $\geq$100 m).

ACKNOWLEDGMENTS. We thank Jay Fein and the National Science Foundation (NSF) for their invaluable support in developing the Unmanned Aerial Vehicles program; H. Nguyen, D. Fahey, J. Kuettner, C. Jennison, and R. Curry for their insight in preparing and conducting MAC and the flight crew from Advanced Ceramics for the field support; the Maldivian Department of Meteorology, Hanimaadhoo Island Office, and Island Aviation for their assistance and logistical support; and J. Coakley, G. Feingold, and P. Chylek for thoughtful reviews and comments that significantly contributed to the overall quality of this manuscript. This work was supported by NSF, National Oceanic and Atmospheric Administration, and National Aeronautics and Space Administration.

1. Charlson RJ, *et al.* (1992) Climate forcing by anthropogenic aerosols. *Science* 255:423–430.
2. Twomey S (1974) Pollution and planetary albedo. *Atmos Environ* 8:1251–1256.
3. Albrecht BA (1989) Aerosols, cloud microphysics, and fractional cloudiness. *Science* 245:1227–1230.
4. IPCC (2007) *4th Assessment Report of the Intergovernmental Panel on Climate Change* (IPCC, Geneva).
5. Köhler H (1936) The nucleus in and the growth of hygroscopic droplets. *Trans Faraday Soc* 32:1152–1161.
6. Twomey S, Warner J (1967) Comparison of measurements of cloud droplets and cloud nuclei. *J Atmos Sci* 24:702–703.
7. Lee IY, Pruppacher HR (1977) Comparative-study on growth of cloud drops by condensation using an air parcel model with and without entrainment. *Pure Appl Geophys* 115:523–545.
8. Snider J, Brenguier J (2000) Cloud condensation nuclei and cloud droplet measurements during ACE-2. *Tellus* 52:828–842.
9. Leaitch WR, *et al.* (1996) Physical and chemical observations in marine stratus during the 1993 North Atlantic Regional Experiment: Factors controlling cloud droplet number concentrations. *J Geophys Res* 101:29123–29135.
10. Warner J, Twomey S (1967) The production of cloud nuclei by cane fires and the effect on cloud drop concentrations. *J Atmos Sci* 24:704–706.
11. Hudson JG (1983) Effects of CCN concentrations on stratus clouds. *J Atmos Sci* 40:480–486.
12. Martin GM, Johnson DW, Spice A (1994) The measurement and parameterization of effective radius of droplets in warm stratocumulus clouds. *J Atmos Sci* 51:1823–1842.
13. Wilcox E, Roberts G, Ramanathan V (2006) Influence of aerosols on the shortwave cloud radiative forcing from North Pacific oceanic clouds: Results from the Cloud Indirect Forcing Experiment (CIFEX). *Geophys Res Lett* 33:L21804.
14. Radke LF, Coakley JA, King MD (1989) Direct and remote sensing observations of the effects of ships on clouds. *Science* 246:1146–1149.
15. Han QY, Rossow WB, Zeng J, Welch R (2002) Three different behaviors of liquid water path of water clouds in aerosol-cloud interactions. *J Atmos Sci* 59:726–735.
16. Twohy CH, *et al.* (2005) Evaluation of the aerosol indirect effect in marine stratocumulus clouds: Droplet number, size, liquid water path, and radiative impact. *J Geophys Res* 110:D08203.
17. Brenguier JL, Pawlowska H, Schuller L (2003) Cloud microphysical and radiative properties for parameterization and satellite monitoring of the indirect effect of aerosol on climate. *J Geophys Res* 108:8632.
18. Bohren CF, Battan LJ (1980) Radar backscattering by inhomogeneous precipitation particles. *J Atmos Sci* 37:1821–1827.
19. Ramanathan V, *et al.* (2007) Warming trends in Asia amplified by brown cloud solar absorption. *Nature* 448:575–578.
20. Heymsfield AJ, McFarquhar GM (2001) Microphysics of INDOEX clean and polluted trade cumulus clouds. *J Geophys Res* 106:28653–28673.
21. Corrigan C, Roberts G, Ramana M, Kim D, Ramanathan V (2008) Capturing vertical profiles of aerosols and black carbon over the Indian Ocean using autonomous unmanned aerial vehicles. *Atmos Chem Phys* 8:737–747.
22. Roberts G, Mauger G, Hadley O, Ramanathan V (2006) North American and Asian aerosols over the Eastern Pacific Ocean and their role in regulating cloud condensation nuclei. *J Geophys Res* 111:D13205.
23. Hoppel WA, Frick GM, Fitzgerald JW (1996) Deducing droplet concentration and supersaturation in marine boundary layer clouds from surface aerosol measurements. *J Geophys Res* 101:26553–26565.
24. Hudson JG (1982) Correlation between surface and cloud base CCN spectra in Montana. *J Appl Meteorol* 21:1427.
25. Roberts GC, Artaxo P, Zhou JC, Swietlicki E, Andreae MO (2002) Sensitivity of CCN spectra on chemical and physical properties of aerosol: A case study from the Amazon Basin. *J Geophys Res* 107:8070.
26. McFarquhar GM, Heymsfield AJ (2001) Parameterizations of INDOEX microphysical measurements and calculations of cloud susceptibility: Applications for climate studies. *J Geophys Res* 106:28675–28698.
27. Ackerman AS, *et al.* (2000) Effects of aerosols on cloud albedo: Evaluation of Twomey's parameterization of cloud susceptibility using measurements of ship tracks. *J Atmos Sci* 57:2684–2695.
28. Platnick S, Twomey S (1994) Determining the susceptibility of cloud albedo to changes in droplet concentration with the advanced very high-resolution radiometer. *J Appl Meteorol* 33:334–347.
29. Pincus R, Baker MB (1994) Effect of precipitation on the albedo susceptibility of clouds in the marine boundary layer. *Nature* 372:250–252.
30. Xue HW, Feingold G (2006) Large-eddy simulations of trade wind cumuli: Investigation of aerosol indirect effects. *J Atmos Sci* 63:1605–1622.
31. Ramanathan V, *et al.* (2001) Indian Ocean Experiment: An integrated analysis of the climate forcing and effects of the great Indo-Asian haze. *J Geophys Res* 106:28371–28398.
32. Paluch IR, Knight CA (1984) Mixing and the evolution of cloud droplet size spectra in a vigorous continental cumulus. *J Atmos Sci* 41:1801–1815.
33. Baker MB, Latham J (1979) Evolution of droplet spectra and the rate of production of embryonic raindrops in small cumulus clouds. *J Atmos Sci* 36:1612–1615.
34. Baker MB, Corbin RG, Latham J (1980) The influence of entrainment on the evolution of cloud droplet spectra: 1. A model of inhomogeneous mixing. *Q J R Meteor Soc* 106:581–598.
35. Baker BA (1992) Turbulent entrainment and mixing in clouds—A new observational approach. *J Atmos Sci* 49:387–404.
36. Ackerman AS, Kirkpatrick MP, Stevens DE, Toon OB (2004) The impact of humidity above stratiform clouds on indirect aerosol climate forcing. *Nature* 432:1014–1017.
37. Wen GY, Marshak A, Cahalan RF, Remer LA, Kleidman RG (2007) 3-D aerosol–cloud radiative interaction observed in collocated MODIS and ASTER images of cumulus cloud fields. *J Geophys Res* 112:D13204.
38. Brenguier J, Fouquart Y, Schüller L (2000) Radiative properties of boundary layer clouds: Optical thickness and effective radius versus geometrical thickness and droplet concentration. *J Atmos Sci* 57:803–821.
39. Duda DP, Stephens GL, Stevens B, Cotton WR (1996) Effects of aerosol and horizontal inhomogeneity on the broadband albedo of marine stratus: Numerical simulations. *J Atmos Sci* 53:3757–3769.
40. Cahalan RF, Ridgway W, Wiscombe WJ, Bell TL, Snider JB (1994) The albedo of fractal stratocumulus clouds. *J Atmos Sci* 51:2434–2455.
41. Corrigan CE, Ramanathan V, Schauer JJ (2006) Impact of monsoon transitions on the physical and optical properties of aerosols. *J Geophys Res* 111:D18208.
42. Ramana MV, Ramanathan V (2006) Abrupt transition from natural to anthropogenic aerosol radiative forcing: Observations at the ABC–Maldives Climate Observatory. *J Geophys Res* 111:D20207.
43. Roberts G, Nenes A (2005) A continuous-flow streamwise thermal-gradient CCN chamber for airborne measurements. *Aero Sci Tech*, 206–221.
44. Ramana M, Ramanathan V, Kim D, Roberts G, Corrigan C (2007) Albedo, atmospheric solar absorption, and atmospheric heating rate measurements with light weight autonomous stacked UAVs. *Q J R Meteorol Soc* 133:1913–1931.